Translational Oncology
www.transonc.com

Volume 4 Number 1 February 2011 pp. 29–37 29

Potential Role of Coregistered Photoacoustic and Ultrasound Imaging in Ovarian Cancer Detection and Characterization[1]

Andres Aguirre*, Yasaman Ardeshirpour*, Mary M. Sanders†, Molly Brewer‡ and Quing Zhu*

*Biomedical Ultrasonic and Optical Imaging Laboratory, Electrical and Computer Engineering Department, University of Connecticut, Storrs, CT, USA; †Department of Pathology and Laboratory Medicine, University of Connecticut Health Center, Farmington, CT, USA; ‡The Carole and Ray Neag Comprehensive Cancer Center, University of Connecticut Health Center, Farmington, CT, USA

Abstract

Currently, there is no adequate technology to detect early stage ovarian cancers. Most of the cancers in the ovary are detected when the cancer has already metastasized to other parts of the body. As a result, ovarian cancer has the highest mortality of all gynecologic cancers with a 5-year survival rate of 30% or less. Thus, there is an urgent need to improve the current diagnostic techniques. Photoacoustic imaging (PAI) is an emerging modality with a great potential to assist ultrasound for detecting ovarian cancer noninvasively. In this article, we report the first study of coregistered ultrasound and PAI of 33 *ex vivo* human ovaries. An assessment of the photoacoustic images has revealed light absorption distribution in the ovary, which is directly related to the vasculature distribution and amount. Quantification of the light absorption levels in the ovary has indicated that, in the postmenopausal group, malignant ovaries showed significantly higher light absorption than normal ones ($P = .0237$). For these two groups, we have obtained a sensitivity of 83% and a specificity of 83%. This result suggests that PAI is a promising modality for improving ultrasound diagnosis of ovarian cancer.

Translational Oncology (2011) 4, 29–37

Introduction

Cancer of the ovary has the lowest survival rate of all the gynecologic cancers, with a 5-year survival rate of 30% or less [1,2]. Because of the high mortality associated with ovarian cancer, most women with a screening abnormality will undergo oophorectomy with at most 2% risk of having ovarian cancer [3]. With the current screening and diagnostic abilities, we will continue to diagnose most women with ovarian cancer (70%) at stage III or IV of the disease (widespread intra-abdominal disease) and most of them will die of their disease. By contrast, stage I cancers have a 5-year survival of 80% to 90%. Technology capable of reliably diagnosing ovarian cancer in earlier stages or before the development of invasive disease could reduce the high mortality and the large economic impact of this disease, particularly in high-risk women. An even larger impact would result from those women who could avoid surgery because they could be assured that an ovarian mass was not cancer.

In 2002, two landmark studies [4,5] were published on the benefit of prophylactic oophorectomy (PO), and it has become accepted as the standard of care for women carrying the BRCA1 or 2 mutation. Since then, PO has reduced the risk of ovarian cancer by more than 50% in these patients. In the absence of reliable methods for the early detection of ovarian cancer, PO has been proposed as the most effective way to prevent this potentially lethal disease in this high-risk group of women [6,7]. Although PO is effective in preventing breast and ovarian cancer, there seems to be a higher mortality for premenopausal oophorectomy, and these high-risk women are not candidates for hormone replacement therapy because of their increased

Address all correspondence to: Quing Zhu, PhD, University of Connecticut, Electrical and Computer Engineering, 371 Fairfield Way; U-2157, Storrs, CT 06269-2157.
E-mail: zhu@engr.uconn.edu

[1]The authors acknowledge the partial funding support of this work by the University of Connecticut Pilot Grant, National Institutes of Health (R01EB002136), and The Donaghue Medical Research Foundation.
Received 6 July 2010; Revised 27 September 2010; Accepted 28 September 2010

1944-7124/11
DOI 10.1593/tlo.10187

risk of breast cancer. Thus, there is an urgent need for an alternative to PO, which is the major rationale for developing better and more sensitive tools to effectively evaluate the ovary.

Currently, there is no single test for ovarian cancer, and the combination of the serum marker cancer antigen 125 screening (sensitivity of ~50% [8–10]), transvaginal ultrasound (3% positive predictive value [PPV] [11]), and pelvic examinations (sensitivity of <30% [9]) yields low PPV for routine screening. A recent review of imaging technologies used for ovarian cancer surveillance concluded that current imaging modalities are expensive and produce low-yield results [12]. Computed tomographic (CT) scans have been studied extensively for ovarian cancer detection, and multiple studies confirm that CT has a sensitivity of 45% and a specificity of 85%. It is poor in the detection of small metastases less than 2 cm. Magnetic resonance imaging (MRI) has not been shown to have a significant advantage, although it may be slightly more sensitive than CT. A 2003 publication [13] suggested that MRI was superior to CT for characterizing malignant features of an ovarian mass and is often used when ultrasound is not diagnostic. However, the cost of MRI is high and is usually used as secondary imaging method. Positron emission tomography, using ^{18}F-2-fluoro-2-deoxy-D-glucose as a tracer, can detect malignant cancers with altered glucose metabolism and has been used for the assessment of lymph node involvement [14], evaluation of pretreatment staging and treatment response [14,15], and detection of cancer metastases. It also holds promise in more accurate evaluation of recurrent or residual cancers [16] than those morphologic modalities. However, it has limited value in lesion localization in early stages of ovarian cancer because of the difficulty in distinguishing between the signal from early-stage cancers and the background uptake signals coming from the normal tissue [17]. Thus, we have not met the current need for better techniques to interrogate the ovary to rule out cancer.

Photoacoustic imaging (PAI) is an emerging biomedical imaging technique in which a short-pulsed laser beam penetrates diffusely into a tissue sample [18–21]. The transient acoustic waves, or photoacoustic waves arising from thermoelastic expansion resulting from a transient temperature rise (on the order of 10 mK), are then measured outside the sample by wide-band ultrasound transducers. The acquired photoacoustic waves are used to reconstruct, at ultrasound resolution, the light absorption distribution that reveals optical contrast, which is directly related to microvessel density of tumors or tumor angiogenesis [22]. Angiogenesis is a key and very early process for tumor growth and metastasis [22,23]. In addition, if two optical wavelengths are used, the measured photoacoustic signals can be used to reconstruct the distribution of tumor hypoxia, which is an important and also very early indicator of tumor metabolism and therapeutic response. These functional parameters are critical in the initial diagnosis of a tumor and the assessment of tumor response to treatment. Because of intense light scattering in tissue, to date, pure optical methods require direct contact with the ovary, which necessitates an invasive procedure to access the ovary [24,25]. PAI minimizes the deleterious effects of intense light scattering by measuring ultrasonic waves generated from the tissue; therefore, it has great potential to noninvasively reveal functional information about the ovary. Provided that enough light fluency is delivered, the penetration depth of PAI is scalable with ultrasound frequency. In the diagnostic frequency range of 3 to 8 MHz, the penetration depth in tissue can reach 3 cm using NIR light [26], which is comparable with the penetration depth used in conventional transvaginal ultrasound.

Coregistered ultrasound and PAI allows visualization of tumor structure and functional changes simultaneously, which may potentially reveal early tumor angiogenesis development that is not available by ultrasound alone. The ability to detect early angiogenesis changes, as well as tumor morphology changes in the ovary, using a noninvasive imaging modality will greatly enhance the care for women.

In the past, we reported, for the first time, characterization results of normal *ex vivo* ovarian tissue from pigs using a three-dimensional coregistered ultrasound and PAI system [27,28]. The results showed strong light absorption from highly vascularized corpora lutea and low absorption from follicles, demonstrating that PAI is capable of detecting vascularized structures in the ovary otherwise not visible with ultrasound. In this article, we present the first imaging results from *ex vivo* human ovaries consisting of normal, abnormal and malignant ovarian tissue. The *ex vivo* imaging assessment is a necessary step toward translating this technology into *in vivo* clinical studies. Our initial results indicate that PAI aided with ultrasound is capable of differentiating normal ovaries from malignant ones based on light absorption levels and distribution patterns.

Materials and Methods

Ovaries were extracted from patients undergoing oophorectomy at the University of Connecticut Health Center. The patients were at risk for ovarian cancer and were undergoing prophylactic surgery or had an ovarian mass suggestive of a malignancy. The institutional review board of the University of Connecticut Health Center approved this study, and informed consent was obtained from all patients. Ovaries were kept in a 0.9% wt/vol NaCl solution immediately after they were excised and imaged within 24 hours after extraction. After imaging experiments, the ovaries were fixed in formalin and returned to the Pathology Department for histologic processing. For histologic evaluation, the ovaries were cut into 5-mm blocks parallel to the imaging plane, dehydrated with graded alcohol, embedded in paraffin, and sectioned into 7-μm thickness using a paraffin microtome. Once the slides that correspond to the imaged planes were identified, they were stained using hematoxylin and eosin (H&E) and CD31 immunostaining.

A coregistered ultrasound and PAI system, designed and developed in our laboratory, was used to image the ovaries. The details of the system can be found in our earlier publications [27,28]. Briefly, the system consists of a 1.75-dimensional ultrasound array capable of providing multiple ultrasound pulse-echo B-Scan images within 80- and 20-degree angles in the lateral and elevation directions, respectively, which is suitable for *ex vivo* imaging of ovaries. The array has a nominal center frequency of 5 MHz with 60% bandwidth. In PAI mode, a tunable Ti-Sapphire laser (Symphotics TII, LS-2134; Symphotics, Camarillo, CA), optically pumped with a Q-switched Nd:YAG laser (Symphotics-TII, LS-2122), was used to illuminate the samples. The laser, set to emit at 740 nm for this study, delivered 12-nanosecond pulses at a rate of 15 Hz. The beam was diverged with a planoconcave lens and homogenized by a circular profile engineered diffuser (ED1-S20; ThorLabs, Newton, NJ) to produce a uniform illumination beam on the sample of approximately 3 cm in diameter. The laser power was limited to 4 mJ/cm^2, which is well below the ANSI limit [29]. The 1.75-dimensional ultrasound array system is capable of switching from ultrasound pulse-echo mode to photoacoustic mode, providing coregistered ultrasound and photoacoustic images. Both the ultrasound and photoacoustic images were reconstructed using a typical delay and sum algorithm based on the transducer array geometry.

During imaging, the 1.75-dimensional transducer and the sample were submerged in 0.9% NaCl solution. All the ovaries were placed approximately in the same location inside the field of view, close to the elevation focus of the transducer array in the axial direction and centered in the azimuth direction. A diagram of the imaging setup is shown in Figure 1. For most ovaries, several images were taken. In the cases where the ovary was bigger than the illumination beam, the images were acquired at different locations to cover most of it.

Ultrasound images were plotted on a gray scale, and photoacoustic images were plotted using a color scale. In both cases, the brightest colors indicate stronger signals. As a means to provide structural guidance to the photoacoustic images, the obtained ultrasound and photoacoustic images were superimposed. In addition, to compare the PAI results from all ovaries, we have ranked each ovary based on the detected photoacoustic signal strength. This was accomplished by defining a parameter named average maximum RF signal (AMRFS), which was computed for each imaging experiment and is given by:

$$\mathrm{AMRFS} = 100 \times \frac{\sum_{i=1}^{\mathrm{TxNumEl}} \max[p_i(t)]}{\mathrm{TxNumEl}}$$

where TxNumEl = 1280 is the number of elements in the ultrasound transducer array and $p_i(t)$ is the measured photoacoustic signal at transducer element i. For the cases where several imaging experiments were performed per ovary, an average of the AMRFS values was used to rank each ovary. In that way, the averaged AMRFS parameter provides an estimate of the overall level of light absorption for each ovary. Because imaging was performed in a low absorbing medium, no ovarian tissue and background boundary had to be defined to compute the AMRFS from the measured signals. Nevertheless, transients from the front face of the ultrasound transducer were removed before computation of the parameter.

A two-sample t test was used to calculate significance for comparisons between groups. A difference with a P value of .05 was considered to be statistically significant. To estimate the sensitivity and specificity, a threshold was retrospectively selected as the average of AMRFS of all ovaries to separate most malignant ovaries from the postmenopausal normal ovaries. False-negative results were malignant ovaries with AMRFS lower than the threshold, and false-positive results were normal ovaries with AMRFS higher than the threshold. The sensitivity and specificity were calculated as: Sensitivity = TP × 100 / (TP + FN); specificity = TN × 100 / (TN + FP), where TP is true-positive findings, TN is true-negative findings, FP is false-positive findings, and FN is false-negative findings. In addition, the positive predictive value was computed as PPV = TP × 100 / (TP + FP).

Results

A total of 33 ovaries from 24 patients (aged 38-83 years; mean, 58 years) were imaged using the coregistered ultrasound and PAI system. All premenopausal ovaries (n = 8) were diagnosed as normal, whereas postmenopausal ovaries were diagnosed as normal (n = 6), abnormal (n = 11), and malignant (n = 8). The group of ovaries with abnormal diagnosis included ovaries with adenofibroma, necrotic fibrothecoma, fibroma, and ovaries from patients with carcinosarcoma or endometrial cancer in the uterus or contralateral ovarian cancer. For the malignant group, five of the samples were a portion of the whole ovary as part of each ovary had to go for frozen section. Four of the five pieces were larger than 4 cm and were included in the data analysis. One small piece of less than 1 cm was removed from the analysis because of significant blood loss in the sample. Therefore, it may not represent the hemoglobin content of the intact ovary. One ovary in the malignant group had few cancer cells on the surface which were likely transported from her 10-cm pelvic carcinosarcoma mass through bloodstream and was removed from data analysis. In addition, one necrotic fibrothecoma sample in the abnormal group consisted of dead tissue and was removed from the data

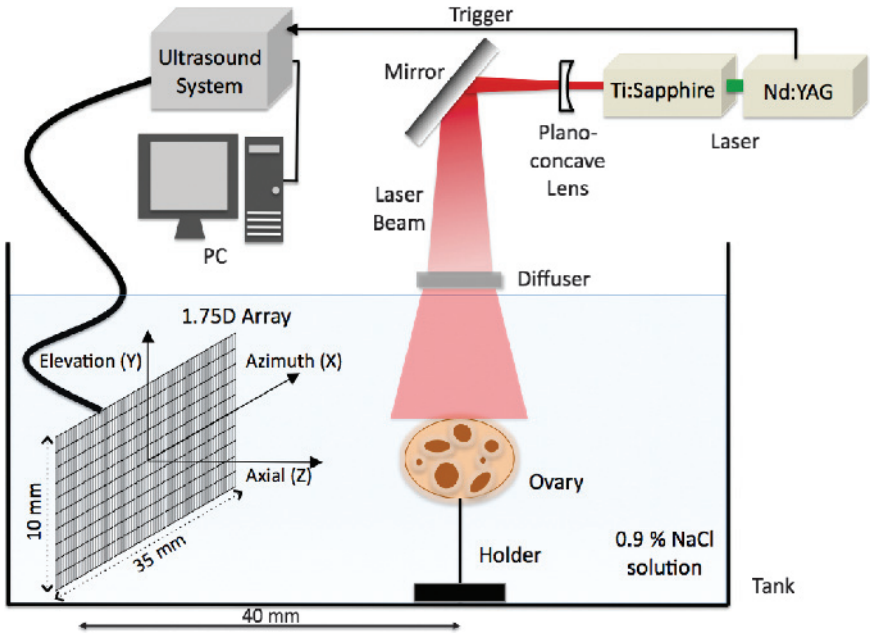

Figure 1. Experimental setup used for imaging *ex vivo* ovaries with the coregistered ultrasound and PAI system. Reproduced from Aguirre et al. [28] with permission.

Table 1. Diagnostic and Measurement Summary of the Imaged Ovaries.

Patient No.	Ovary	Age, years	Status	Diagnostic	Lowest AMRFS	Mean AMRFS	Peak AMRFS	Mean AMRFS	SD AMRFS
5	5	38	Pre	Normal	2.33	3.11	3.84	2.95	0.58
6	6	44			1.99	1.99	1.99		
8	8	46			2.05	2.40	2.63		
10	11	47			2.68	2.93	3.40		
17	20	47			1.89	3.34	4.04		
17	21	47			3.54	3.62	3.71		
21	28	41			2.12	2.61	3.22		
22	29	43			2.23	3.57	6.21		
1	1	58	Post	Normal	2.19	2.19	2.20	2.39	0.50
4	4	53			1.84	1.84	1.84		
12	13	64			2.16	2.35	2.66		
13	15	72			1.94	1.99	2.04		
20	27	59			2.83	3.18	3.37		
24*	33	54			2.37	2.77	3.16		
2	2	78	Post	Carcinosarcoma in the uterus	1.85	1.85	1.85	2.82	0.90
3	3	58		Endometrial cancer	2.03	2.03	2.03		
7	7	55		Endometrial cancer	3.14	4.31	5.48		
9*	9	50		Endometrial cancer	1.92	1.99	2.05		
9*	10	50		Endometrial cancer	2.04	2.05	2.07		
14	16	52		Adenofibroma	1.92	3.45	6.99		
16*	22	75		Ovarian cancer in other side	2.91	3.02	3.14		
19*	25	60		Endometrial cancer	3.30	3.51	3.84		
19*	26	60		Endometrial cancer	3.14	3.81	4.51		
24*	32	54		Fibroma	1.96	2.21	2.58		
15*	17	58	Post	High-grade cancer on other ovary	4.42	5.08	6.21	3.55	0.89
15*	18	58		High-grade cancer	3.33	3.92	5.22		
16*	19	75		Low-grade cancer	2.06	2.63	4.03		
18	23	50		High-grade cancer	1.82	3.05	4.89		
23*	30	55		Intermediate-grade cancer	1.93	2.99	4.61		
23*	31	55		Intermediate-grade cancer	1.98	3.63	6.09		

*Indicates patients whose both ovaries were studied.

analysis. A summary of the diagnosis of the remaining 30 ovaries is given in Table 1.

Examples of Coregistered Ultrasound and PAI

Figure 2 (*A* and *B*) represents ultrasound and coregistered ultrasound and photoacoustic images of a 38-year-old high-risk woman with enlarged ovaries found from clinical screening ultrasound (no. 5 in Table 1). The ultrasound image reveals the presence of several antral follicles, which are typical of normal premenopausal ovaries. In addition, the photoacoustic image indicates that most of the light absorption takes place in the theca, which surrounds the antral follicle and is rich in vasculature. The source of the light absorption is the presence of blood in the theca, which volume depends on the current stage of the development of the follicle. Histologic evaluation of the sample revealed a normal premenopausal ovary (Figure 2*C*). Immunostaining with CD31 revealed scattered microvessels in the

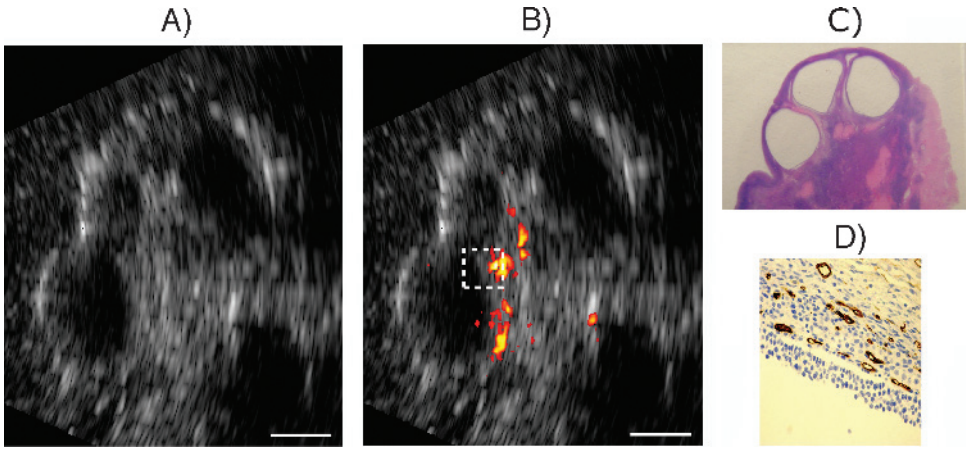

Figure 2. Imaging of a normal premenopausal ovary. (A) Ultrasound image. (B) Coregistered ultrasound and photoacoustic image. (C) H&E staining of the corresponding area (×1). (D) Immunostaining (CD31, ×100) revealing microvessels in the theca around the follicles from the rectangular region indicated in B. White bar, 5 mm.

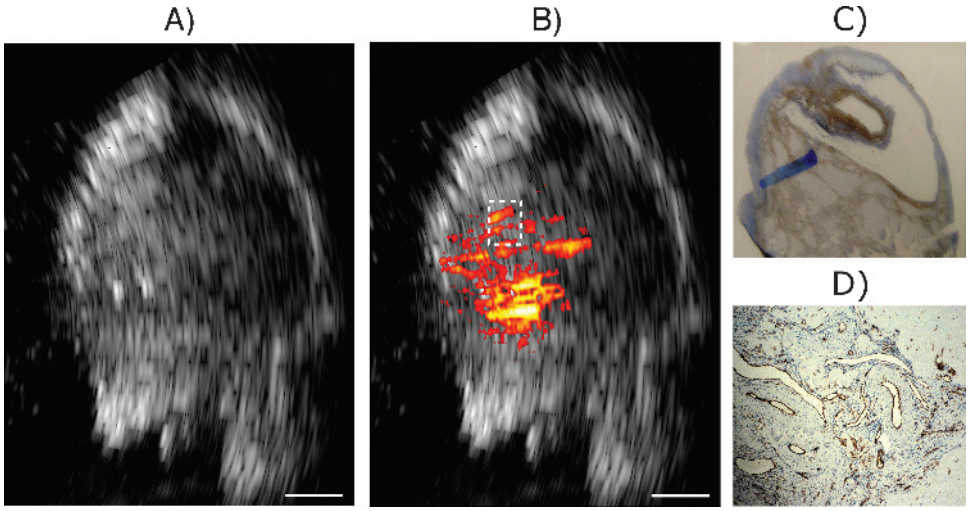

Figure 3. Imaging of an abnormal postmenopausal ovary from a patient with endometrial cancer. (A) Ultrasound image. (B) Coregistered ultrasound and photoacoustic image. (C) Immunostaining (CD31) of the corresponding area (×1). (D) Immunostaining (×100) of the highly vascularized area showing a cluster of small arteries from the rectangular region indicated in B. White bar, 5 mm.

theca around the follicles (Figure 2*D*). On the contrary, ultrasound and photoacoustic images of the normal postmenopausal ovaries, in general, were lacking follicles, and the light absorption across the entire ovary was low.

An example of an abnormal ovary (no. 7 in Table 1) from a 55-year-old postmenopausal patient with endometrial cancer is shown in Figure 3. The photoacoustic image reveals a highly vascularized area compared with the surrounding tissue. The H&E staining of the corresponding region showed a high density of small vessels; however, no malignant cells were found in the ovary. CD31 staining (Figure 3*C*) revealed a cluster of randomly distributed small thick-walled irregular arteries in the corresponding area. We hypothesize that the endometrial cancer may have increased the overall vascularity to the reproductive tract. Another scenario is that there was micrometastases to the ovary not identified on the histologic section.

Coregistered images of a malignant ovary (no. 17 in Table 1) from a 58-year old postmenopausal woman with bilateral ovarian cancers at stage IIIC are shown in Figure 4. Images from two areas are shown in Figure 4 (*B* and *C*). High intraepithelial vascular areas compared with the surrounding tissue are observed in the photoacoustic images. The H&E staining of the corresponding regions showed high-grade carcinoma (Figure 4, *B1* and *C1*) and immunostaining with CD31 (Figure 4, *B2* and *C2*) showed extensive thin-walled microvessels in the corresponding regions.

Quantitative Analysis

We computed the average AMRFS value for each ovary. The scatter plot in Figure 5 shows the average AMRFS values of all ovaries from the four different groups. The results indicate the overall higher light absorption levels in malignant postmenopausal ovaries than in any other ovaries. Normal postmenopausal ovaries have, in general, the lowest average AMRFS values. For these two groups of ovaries, normal postmenopausal *versus* malignant postmenopausal, the sensitivity and specificity are 83% (5/6) and 83% (5/6), respectively. The PPV is 83% (5/6), which is a significant improvement to ultrasound alone in current clinical practice. In the case of the abnormal postmenopausal group, a wide variation of the average AMRFS is observed among these ovaries. This can be explained by the fact that this group consists of different types of abnormalities with different amounts of vascular content. Similarly, normal ovaries in the premenopausal group exhibit some degree of variation, which can be attributed to different stages in the menstrual cycle at the time of the surgery.

The mean AMRFS value for each postmenopausal group, along with their standard deviation, is shown in Figure 6. A two-sample *t* test showed statistical significance between normal (mean AMRFS = 2.39 ± 0.50, $n = 6$) and malignant (mean AMRFS = 3.55 ± 0.89, $n = 6$) postmenopausal ovaries ($P = .0237$). A *t* test between normal and abnormal plus malignant (mean AMRFS = 3.10 ± 0.94, $n = 16$) postmenopausal ovaries also showed statistical significance ($P = .0368$). However, there was no statistical significance between normal and abnormal ovaries ($P = .2361$) or between abnormal and malignant ($P = .1438$) postmenopausal groups. Certainly, the sample sizes for all groups are small in this pilot study. However, the results from the normal and malignant postmenopausal groups are promising and warrant further investigation.

Although, no abnormal or malignant premenopausal ovaries were imaged in this study, we have compared the normal premenopausal ovaries with normal postmenopausal ones as shown in Figure 7. No statistical significance between the two groups was found ($P = .08$).

Discussion

We have shown that PAI of normal *ex vivo* human ovaries provides different light absorption distribution maps between premenopausal and postmenopausal ovaries. Aided by morphologic information from coregistered ultrasound images, the light absorption distribution in the photoacoustic images could improve the diagnosis of an ovarian abnormality and potentially predict the risk of cancer. When comparing the images from the normal premenopausal and postmenopausal groups, the differences between the two groups are clear, both in ultrasound and photoacoustic images. In the ultrasound images, several antral follicles are visible in the premenopausal ovaries, whereas little to no follicular activity is observed in the postmenopausal ovaries. Similarly, the photoacoustic images show areas

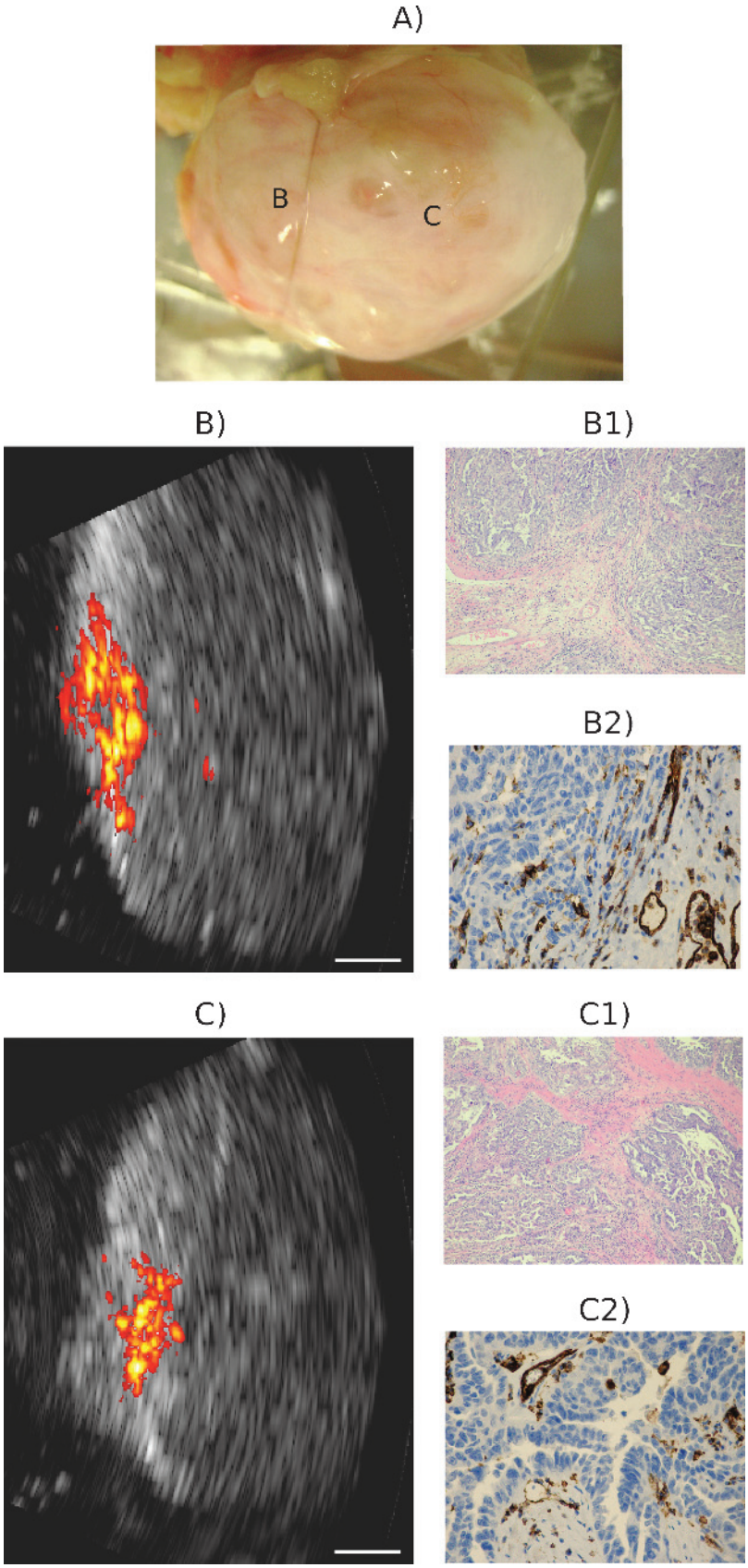

Figure 4. Imaging of a malignant postmenopausal ovary. (A) Coregistered ultrasound and photoacoustic images of two different locations are shown in B and C. (B1 and C1) H&E stains (×40) of the corresponding areas showing extensive high-grade tumors. (B2 and C2) CD31 stains (×100) of the corresponding areas showing extensive thin-walled microvessels. White bar, 5 mm.

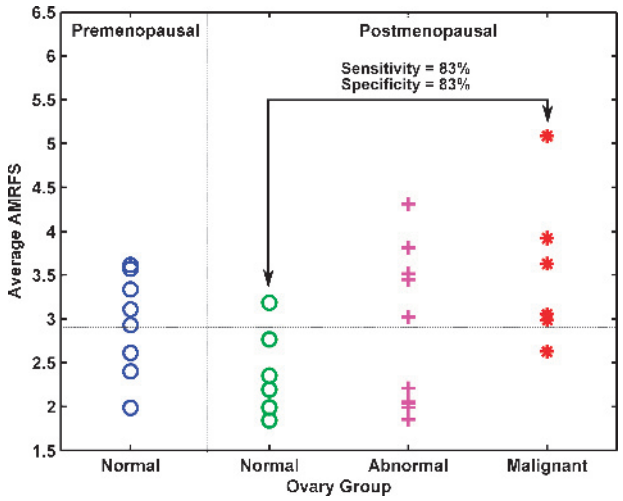

Figure 5. Scatter plot of the measured AMRFS values of four groups. The vertical axis is the AMRFS, and the horizontal axis presents four groups. A threshold is chosen as the average of all the AMRFS measurements of all ovaries. For the postmenopausal group, the sensitivity and specificity between normal and malignant ovaries is 83%.

of high light absorption around the follicles in the premenopausal ovaries and low light absorption across the postmenopausal ovaries. More specifically, when comparing the results among postmenopausal subgroups (normal, abnormal, and malignant), marked differences have been identified in the photoacoustic images. The light absorption distribution from ovaries in the abnormal group varied more than in the malignant ovaries, which showed more consistent results within their group, suggesting this will be an important feature of malignancy because of tumor angiogenesis. High light absorption from ovaries in this group was observed mostly intraepithelial, corresponding to epithelial-derived ovarian tumors, which constitute the predominant and most lethal forms of the disease [30]. In general, abnormal and malignant ovaries were much bigger than normal ones as observed from the ultrasound images. Unfortunately, only normal premenopausal ovaries where available for this study, partially because of the somewhat rare occurrence of premenopausal ovarian cancer and partially because of the high rate of prophylactic oophorectomy for women at risk for ovarian cancer in our patient population; hence, no images from premenopausal ovaries with different pathologic conditions were available. These results demonstrate that PAI combined with ultrasound could greatly improve the diagnosis of ovaries clinically, especially in postmenopausal women where the ovaries are less active and variations due to menstrual cycle changes are not present.

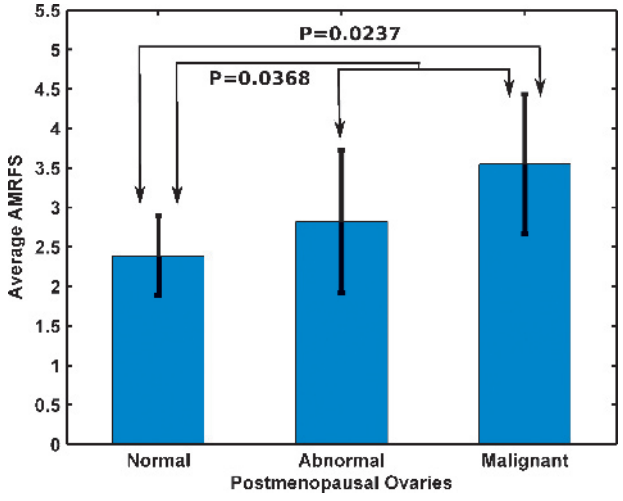

Figure 6. Statistics of AMRFS of all subgroups of postmenopausal ovaries. Statistical significance between normal and malignant ovaries is shown, as well as between normal and abnormal and malignant.

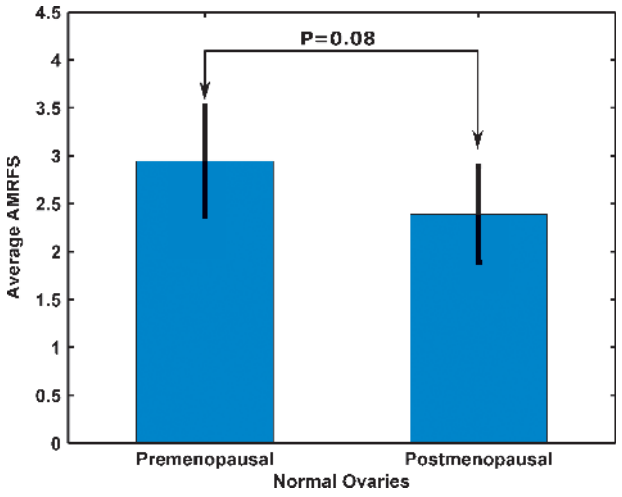

Figure 7. Statistics of AMRFS of all normal ovaries.

We further analyzed the results from the imaging experiments by using the AMRFS parameter. The goal was to have, for a given ultrasound transducer and controlled imaging conditions, a means to compare the light absorption levels from all ovaries. We chose to define this parameter from the unprocessed received signals, instead of from the formed images, to avoid limiting the scope of the parameter to just the planes where the images were formed. Nevertheless, the considered signals were time-limited to avoid inclusion of transients from the front face of the ultrasound transducer. Performing the study in *ex vivo* ovaries presented both advantages and disadvantages. We had control over the imaging conditions, such as using orthogonal illumination, nonabsorbing background (both not available *in vivo*) to minimize result interpretation errors. However, by extracting the ovaries, their blood content was reduced because of bleeding, which directly affected the measurements. This was true in all the studied ovaries; however, in most malignant cases, the ovaries had to be divided and a portion submitted immediately for frozen-section pathologic evaluation of tumor receptors and tumor banking. This further accentuated the blood loss in the samples imaged. Nevertheless, the results showed that the malignant group has the highest AMRFS values. It is likely that the *in vivo* vascular contrast of the malignant group would be higher than that reported in this *ex vivo* study and thus be more sensitive and specific.

A limitation of the photoacoustic technique is that it provides relative optical absorption changes rather than quantitative tissue absorption coefficients. In an effort to correlate the results obtained using the AMRFS to quantitative absorption coefficients of the ovaries, we used a diffuse optical tomography system [31,32] to image the ovaries immediately after the photoacoustic experiments. Diffused light imaging has limited resolution; however, it can reconstruct target optical absorption coefficient μ_a within 60% to 100% accuracy [32,33].

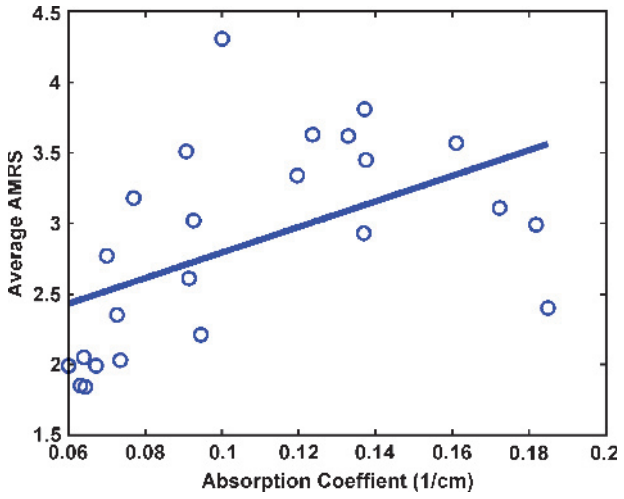

Figure 8. Average AMRFS measured with PAI *versus* absorption coefficient of ovaries imaged with a diffused optical tomography system ($n = 24$). Linear regression analysis obtained a 0.59 correlation coefficient, which is statistically significant ($P < .05$).

The overall reconstructed μ_a for each group of ovaries showed similar trends as those obtained by computing the AMRFS parameter from photoacoustic data. The malignant postmenopausal ovaries had the highest μ_a (0.153 ± 0.037/cm considering whole ovaries only), whereas the normal postmenopausal ovaries had the lowest one (0.069 ± 0.006/cm). Abnormal postmenopausal ovaries again exhibit variable values of μ_a (0.092 ± 0.027/cm) depending on the pathologic condition. The linear regression curve of the average AMRFS *versus* measured absorption coefficient of the 24 whole ovaries imaged with the diffuse optical tomography system was obtained from least square solutions and is shown in Figure 8. The computed correlation coefficient reflecting the goodness of fit was 0.59 with $P = .0023$ at a confidence level of 0.05. Note that diffuse optical tomography is suitable for imaging the entire ovary because the diffused light probes a target from all directions and is sensitive to blood loss at surgical interfaces.

A limitation of the study was the lack of information regarding the menstrual cycle stage at the time of prophylactic oophorectomy on premenopausal patients. Although the number of ovaries in this group was small, variations in AMRFS levels among the ovaries are evident and most likely due to differences in the menstrual cycle or due to differences in the age of the patient. The overall light absorption level obtained from this group was higher than that from the normal postmenopausal group. This was expected because postmenopausal ovaries are less active than premenopausal ones, which have highly vascularized structures such as corpus luteum and corpus hemorrhagicum.

On the basis of our initial results reported in this study, we believe that a combination of light absorption distribution and quantification from photoacoustic images could be used to noninvasively screen postmenopausal women *in vivo* and hence improve the ultrasound diagnosis of ovarian cancer. Implementing this technique requires a coregistered ultrasound and photoacoustic probe that can image the ovaries transvaginally as the standard transvaginal ultrasound. Some potential issues in an *in vivo* setup are the effect of background tissue on light delivery and acoustic attenuation. Not only both of these factors could affect image quality, but their variability in patients would also have to be considered when estimating the light absorption level of the ovaries. However, advantages of an *in vivo* imaging approach are the possibility of measuring the oxygen saturation using two wavelengths and the absence of blood loss due to surgical intervention. From the oxygen saturation measurements, an estimation of tumor hypoxia, which is an important indicator of tumor metabolism and therapeutic response, could be obtained. The biggest advantage, however, is the noninvasive nature of this technology.

Summary

A total of 33 *ex vivo* human ovaries have been studied. Results have shown that PAI of the ovaries provides light absorption distributions that depend on the pathologic condition of the ovary in the postmenopausal group. By comparing the light absorption levels of the ovaries, PAI was capable of diagnosing ovarian cancer from normal postmenopausal ovaries with a sensitivity of 83% and specificity of 83%. Combined with coregistered ultrasound, PAI can potentially improve the current diagnosis of ovarian cancer in postmenopausal women. For premenopausal normal ovaries, our limited data showed no statistically significant difference in light absorption level when compared with normal postmenopausal ovaries. However, no abnormal or malignant premenopausal ovaries were available in this study. The most important finding is that this approach can be easily combined with ultrasound for better performance than ultrasound alone.

Acknowledgments

The authors thank Xiaohong Wang for her help on preparing the pathology slides.

References

[1] Hoskins WJ (1995). Prospective on ovarian cancer: why prevent? *J Cell Biochem Suppl* **23**, 189–199.

[2] American Cancer Society (2009). Cancer facts & figures 2009. *American Cancer Society* **72**.

[3] U.S. Preventive Services Task Force (2004). *Screening for Ovarian Cancer: Recommendation Statement.* http://www.uspreventiveservicestaskforce.org/3rduspstf/ovariancan/ovcanrs.htm.

[4] Kauff ND, Satagopan JM, Robson ME, Scheuer L, Hensley M, Hudis CA, Ellis NA, Boyd J, Borgen PI, Barakat RR, et al. (2002). Risk-reducing salpingo-oophorectomy in women with a BRCA1 or BRCA2 mutation. *N Engl J Med* **346**(21), 1609–1615.

[5] Rebbeck TR, Lynch HT, Neuhausen SL, Narod SA, Van't Veer L, Garber JE, Evans G, Isaacs C, Daly MB, Matloff E, et al. (2002). Prophylactic oophorectomy in carriers of BRCA1 or BRCA2 mutations. *N Engl J Med* **346**(21), 1616–1622.

[6] Fatouros M, Baltoyiannis G, and Roukos DH (2008). The predominant role of surgery in the prevention and new trends in the surgical treatment of women with BRCA1/2 mutations. *Ann Surg Oncol* **15**(1), 21–33.

[7] Kauff ND, Domchek SM, Friebel TM, Robson ME, Lee J, Garber JE, Isaacs C, Evans DG, Lynch H, Eeles RA, et al. (2008). Risk-reducing salpingo-oophorectomy for the prevention of BRCA1- and BRCA2-associated breast and gynecologic cancer: a multicenter, prospective study. *J Clin Oncol* **26**(8), 1331–1337.

[8] NIH Consensus Conference (1995). Ovarian cancer. Screening, treatment, and follow-up. NIH Consensus Development Panel on Ovarian Cancer. *JAMA* **273**(6), 491–497.

[9] Tammela J and Lele S (2004). New modalities in detection of recurrent ovarian cancer. *Curr Opin Obstet Gynecol* **16**(1), 5–9.

[10] Nossov V, Amneus M, Su F, Lang J, Janco JM, Reddy ST, and Farias-Eisner R (2008). The early detection of ovarian cancer: from traditional methods to proteomics. Can we really do better than serum CA-125? *Am J Obstet Gynecol* **199**(3), 215–223.

[11] Goozner M (2010). Personalizing ovarian cancer screening. *J Natl Cancer Inst* **102**(15), 1112–1113.

[12] Shaaban A and Rezvani M (2009). Ovarian cancer: detection and radiologic staging. *Clin Obstet Gynecol* **52**(1), 73–93.

[13] Funt SA and Hricak H (2003). Ovarian malignancies. *Top Magn Reson Imaging* **14**(4), 329–337.

[14] Bristow RE, Giuntoli RL, Pannu HK, Schulick RD, Fishman EK, and Wahl RL (2005). Combined PET/CT for detecting recurrent ovarian cancer limited to retroperitoneal lymph nodes. *Gynecol Oncol* **99**(2), 294–300.

[15] Avril N, Sassen S, Schmalfeldt B, Naehrig J, Rutke S, Weber WA, Werner M, Graeff H, Schwaiger M, and Kuhn W (2005). Prediction of response to neoadjuvant chemotherapy by sequential F-18-fluorodeoxyglucose positron emission tomography in patients with advanced-stage ovarian cancer. *J Clin Oncol* **23**(30), 7445–7453.

[16] Nakamoto Y, Saga T, and Fujii S (2005). Positron emission tomography application for gynecologic tumors. *Int J Gynecol Cancer* **15**(5), 701–709.

[17] Kumar R, Chauhan A, Jana S, and Dadparvar S (2006). Positron emission tomography in gynecological malignancies. *Expert Rev Anticancer Ther* **6**(7), 1033–1044.

[18] Li C and Wang LV (2009). Photoacoustic tomography and sensing in biomedicine. *Phys Med Biol* **54**(19), R59–R97.

[19] Oraevsky A and Karabutov A (2003). Optoacoustic tomography. In *Biomedical Photonics Handbook.* T Vo-Dinh (Ed). CRC Press, Boca Raton, FL. p. 34.

[20] Wang LV (2008). Prospects of photoacoustic tomography. *Med Phys* **35**, 5758–5767.

[21] Xu M and Wang L (2006). Photoacoustic imaging in biomedicine. *Rev Sci Instrum* **77**(4), 041101.

[22] Weidner N, Semple JP, Welch WR, and Folkman J (1991). Tumor angiogenesis and metastasis—correlation in invasive breast carcinoma. *N Engl J Med* **324**(1), 1–8.

[23] Vaupel P, Kallinowski F, and Okunieff P (1989). Blood flow, oxygen and nutrient supply, and metabolic microenvironment of human tumors: a review. *Cancer Res* **49**(23), 6449–6465.

[24] Brewer MA, Utzinger U, Barton JK, Hoying JB, Kirkpatrick ND, Brands WR, Davis JR, Hunt K, Stevens SJ, and Gmitro AF (2004). Imaging of the ovary. *Technol Cancer Res Treat* **3**(6), 617–627.

[25] Hariri LP, Bonnema GT, Schmidt K, Winkler AM, Korde V, Hatch KD, Davis JR, Brewer MA, and Barton JK (2009). Laparoscopic optical coherence tomography imaging of human ovarian cancer. *Gynecol Oncol* **114**(2), 188–194.

[26] Gamelin J, Aguirre A, Maurudis A, Huang F, Castillo D, Wang L, and Zhu Q (2008). Curved array photoacoustic tomographic system for small animal imaging. *J Biomed Opt* **13**(2), 024007.

[27] Aguirre A, Gamelin J, Guo P, Yan S, Sanders M, Brewer M, and Zhu Q (2009). Photoacoustic characterization of ovarian tissue. *Proceedings of SPIE* **7177**(1), 717708.

[28] Aguirre A, Guo P, Gamelin J, Yan S, Sanders MM, Brewer M, and Zhu Q (2009). Coregistered three-dimensional ultrasound and photoacoustic imaging system for ovarian tissue characterization. *J Biomed Opt* **14**(5), 054014.

[29] Z.1.3.6. Committee (2007). *American National Standard for Safe Use of Lasers*. Laser Institute of America, New York, NY.

[30] Karst AM and Drapkin R (2010). Ovarian cancer pathogenesis: a model in evolution. *J Oncol* **2010**, 932371.

[31] Zhu Q, Chen N, and Kurtzman SH (2003). Imaging tumor angiogenesis by use of combined near-infrared diffusive light and ultrasound. *Opt Lett* **28**(5), 337–339.

[32] Zhu Q, Xu C, Guo P, Aguirre A, Yuan B, Huang F, Castilo D, Gamelin J, Tannenbaum S, Kane M, et al. (2006). Optimal probing of optical contrast of breast lesions of different size located at different depths by US localization. *Technol Cancer Res Treat* **5**(4), 365–380.

[33] Xu C, Yuan B, and Zhu Q (2008). Optimal probe design for breast imaging using near-infrared diffused light. *J Biomed Opt* **13**(4), 044002.